# 1

# Metal Oxide Semiconductors: State-of-the-Art and New Challenges

## 1.1 Introduction

Metal oxide semiconductors (MOS) are abundant materials found in the Earth's crust and are commonly used in traditional ceramics. However, they differ significantly from conventional inorganic counterparts like silicon and III–V compounds in various aspects. These distinctions encompass materials design concepts, electronic structure, charge transport mechanisms, defect states, thin-film processing, and optoelectronic properties. As a result, oxide semiconductors enable the realization of both established and innovative functionalities [1].

In comparison to inorganic semiconductors, oxide semiconductors possess unique characteristics. These include exceptional carrier mobilities even in the amorphous state, resilience against mechanical stress, compatibility with organic dielectric and photoactive materials, and high optical transparency. These properties make oxide semiconductors particularly appealing for various applications.

In recent decades, MOS have garnered significant attention in various research fields, including optoelectronics, thin-film transistors (TFTs), photocatalysts, gas sensors, solar cells, and memristors [1–14], as shown in Figure 1.1. MOS can be categorized into two types based on their conductivity: *n*-type, where electrons are the majority carriers, and *p*-type, where holes are the majority carriers. These semiconducting properties arise from factors such as doped aliovalent cations or oxygen nonstoichiometry [15, 16]. Among the *n*-type MOS, ZnO, $SnO_2$, $TiO_2$, $In_2O_3$, and $Ga_2O_3$ are widely studied concerning synthesis, characterization, and applications [17–21]. As for the *p*-type MOS, research efforts primarily focus on $Cu_xO$ (CuO and $Cu_2O$), SnO, and $NiO_x$ [22–24].

## 1.2 *n*-Type Metal Oxide Semiconductors

### 1.2.1 ZnO

Zinc oxide (ZnO), as an *n*-type semiconductor, has sparked significant research interest due to its distinctive physical and chemical properties [25–27]. In the field of materials science, ZnO is classified as a II–VI compound semiconductor, possessing

*Metal Oxide Semiconductors: Synthesis, Properties, and Devices*,
First Edition. Zhigang Zang, Wensi Cai, and Yong Zhou.

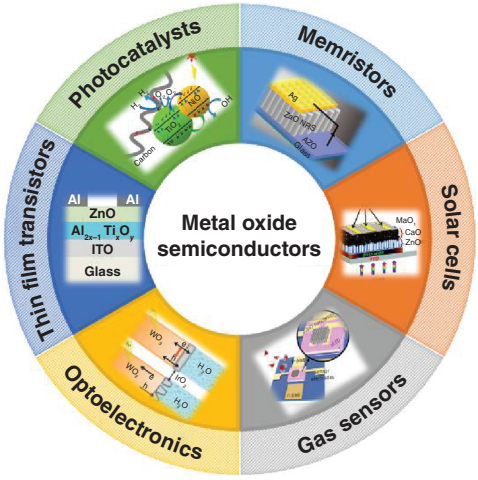


**Figure 1.1** Applications of metal oxide semiconductors. Source: Reprinted with permission from Refs. [9–14]. Copyright 2015 American Chemical Society, 2016 American Chemical Society, 2020 American Chemical Society, 2020 The Royal Society of Chemistry.

a covalence level between ionic and covalent semiconductors. Its attributes, such as a direct wide bandgap ($E_g \sim 3.3$ eV at 300 K), large free exciton binding energy (60 meV), and high thermal and mechanical stability at room temperature, make ZnO a promising candidate for various applications in electronic devices, optoelectronics, gas sensors, and laser technology [28, 29]. Additionally, ZnO can be utilized as an energy collector due to its piezo- and pyroelectric properties, as well as a photocatalyst for hydrogen production [30–32].

The crystal structure of ZnO can be classified into three types: wurtzite (B4), zinc blende (B3), and rocksalt (B1), as shown in Figure 1.2. Thereinto, wurtzite is the most stable thermodynamic phase under ambient conditions. Wurtzite ZnO possesses a hexagonal structure (space group *C*6*mc*) with lattice parameters $a = 0.3296$ nm and $c = 0.52065$ nm. The structure of ZnO can be simply described as a number of alternating planes composed of tetrahedrally coordinated $O^{2-}$ and $Zn^{2+}$ ions, stacked alternately along the c-axis. The tetrahedral coordination in ZnO results in noncentral symmetric structures and consequently piezoelectricity and pyroelectricity [33].

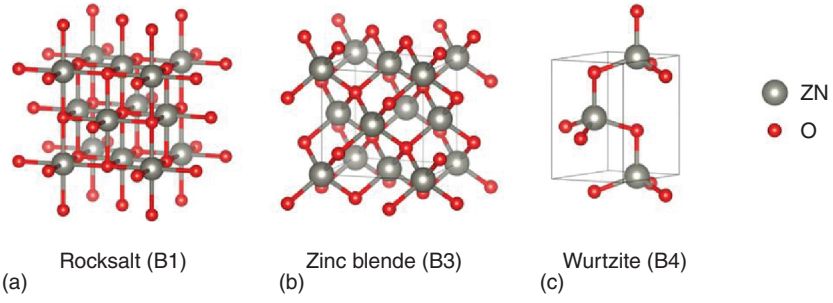


**Figure 1.2** Stick and ball representation of ZnO crystal structures: (a) cubic rocksalt (B1), (b) cubic zinc blende (B3), and (c) hexagonal wurzite (B4). The gray and red spheres denote Zn and O atoms, respectively.

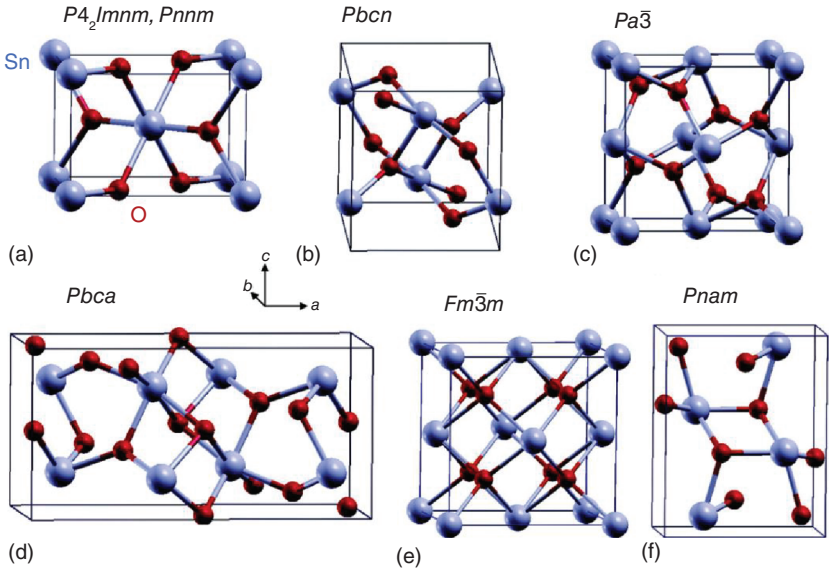


**Figure 1.3** Bulk structures of $SnO_2$ polymorphs (gray and red colors represent Sn and O atoms, respectively). (a) Rutile ($P4_2/mnm$) and $CaCl_2$-type (*Pnnm*), (b) R-$PbO_2$-type (*Pbcn*), (c) pyrite-type ($Pa\bar{3}$), (d) $ZrO_2$-type (*Pbca*), (e) fluorite-type ($Fm\bar{3}hm$), and (f) cotunnite-type (*Pnam*). Source: Reproduced from Gracia et al. [40]/with permission of American Chemical Society.

### 1.2.2 $SnO_2$

$SnO_2$ is also a wide-bandgap (~3.6 eV) *n*-type semiconductor, belongs to the group-IV compounds, and exhibits remarkable transparency and conductivity simultaneously [20, 34, 35]. The unique chemical, electronic, and optical properties of $SnO_2$ have led to extensive research on its applications in various devices, including solar cells [36], catalytic materials [37], and gas sensors [38]. Additionally, $SnO_2$ serves as a distinctive transparent metal oxide and finds wide-ranging applications as transparent conducting oxide electrodes in optoelectronic devices. This is due to its excellent chemical and thermal stabilities in atmospheric environments, as well as its high optical transmission properties [39].

$SnO_2$ possesses several polymorphs including rutile-type ($P4_2/mnm$), $CaCl_2$-type (*Pnnm*), a-$PbO_2$-type (*Pbcn*), pyrite-type ($Pa\bar{3}$), $ZrO_2$-type orthorhombic phase I (*Pbca*), fluorite-type ($Fm\bar{3}m$), and cotunnite-type orthorhombic phase II (*Pnam*) with ninefold coordination, as shown in Figure 1.3. All these structures are sequentially obtained when the most commonly available and stable rutile phase is subjected to a high mechanical pressure [40].

### 1.2.3 $In_2O_3$

Another widely studied *n*-type semiconductor is indium oxide ($In_2O_3$), which has a bandgap ranging from 3.5 to 3.7 eV. It finds numerous applications in electronic

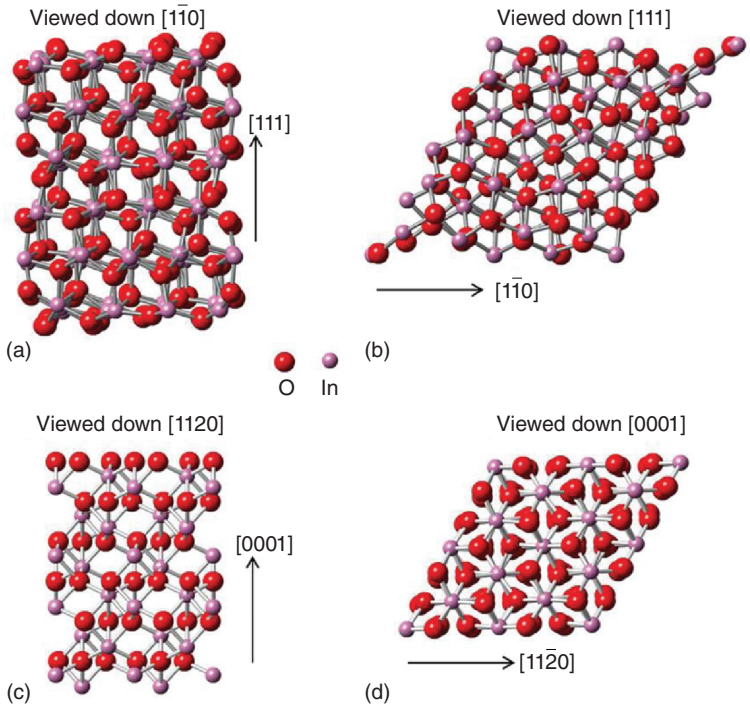


**Figure 1.4** Ball and stick representations of crystal structures of *bcc*-$In_2O_3$ (a, b) and *rh*-$In_2O_3$ (c, d). In atoms are pale pink, and O atoms are dark red. The viewing directions and the in-plane orientation are indicated in the figure. Source: Reproduced from Zhang et al. [42]/with permission of American Chemical Society.

and optoelectronic fields such as solar cells, gas sensors based on TFTs, and Schottky contacts and diodes [21, 41]. $In_2O_3$ can exist in two well-established crystal structures: body-centered cubic (*bcc*) and rhombohedral (*rh*), as depicted in Figure 1.4 [42]. The phase of $In_2O_3$ thermodynamically stable under ambient conditions adopts the body-centered cubic bixbyite structure, with the space group $Ia\bar{3}$ (#206) and a lattice constant of 10.118 Å. The rhombohedral structure is stabilized under high-pressure conditions. The rhombohedral cell belongs to the $R\bar{3}c$ space group with lattice constants $a = 5.478$ Å and $c = 14.51$ Å. There are six formula units per hexagonal cell, and the volume per formula of 62.85 $Å^3$ for the *rh* phase is much smaller than the value of 64.72 $Å^3$ for the ambient *bcc* phase.

### 1.2.4 $TiO_2$

As a member of transition metal oxides, $TiO_2$ is a well-known *n*-type semiconductor [43–46]. It exhibits excellent electronic and optical properties, making it highly suitable for various applications in the fields of gas sensors [47], solar cells [48], and photocatalysis [49]. In its natural form, $TiO_2$ exists in three different

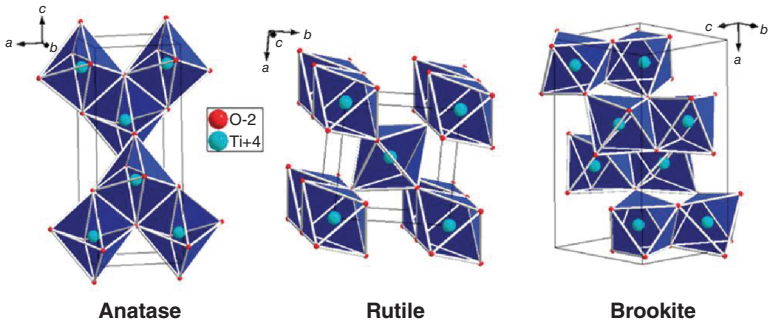


**Figure 1.5** Structure of anatase, rutile, and brookie $TiO_2$. Source: Reproduced from Macwan et al. [51]/with permission of American Chemical Society.

phase structures, namely anatase (tetragonal), brookite (orthorhombic), and rutile (tetragonal), as illustrated in Figure 1.5. These phases have energy bandgaps of 3.2 eV (anatase), 3.02 eV (brookite), and 2.96 eV (rutile) [50, 51]. Among these phases, anatase and rutile are widely applied due to their superior stability, while rutile $TiO_2$, with a tetragonal structure containing six atoms per unit cell, exhibits a slight distortion in the $TiO_6$ octahedron [52]. Anatase $TiO_2$ also possesses a tetragonal structure, but with a slightly larger distortion of the $TiO_6$ octahedron. In general, rutile $TiO_2$ is more thermodynamically stable than anatase under typical temperature and pressure conditions.

### 1.2.5 $Ga_2O_3$

$Ga_2O_3$ is an emerging ultra-wide bandgap semiconductor with a bandgap of 4.8 eV. This unique property enables $Ga_2O_3$ to simultaneously achieve high breakdown voltage and low on-resistance, making it highly promising for both direct current (DC) and radiofrequency (RF) applications [53, 54]. As a result, $Ga_2O_3$ offers exciting prospects in various fields such as electronics (high-power devices, field-effect transistors) [55], optoelectronics (solar cells, solar-blind ultraviolet photodetectors) [56–58], and sensors (gas sensors, radiation detectors) [59]. $Ga_2O_3$ exists in five polymorphs, including corundum ($\alpha$), monoclinic ($\beta$), defective spinel ($\gamma$), orthorhombic ($\delta$), and hexagonal ($\varepsilon$), as shown in Figure 1.6 [53]. Among these, $\beta$-$Ga_2O_3$ is the most stable phase under ambient conditions, while the other phases can transform into $\beta$-$Ga_2O_3$ through heating treatment [60].

## 1.3 *p*-Type Metal Oxide Semiconductors

### 1.3.1 Copper Oxides (CuO/$Cu_2O$)

Tenorite (CuO) and cuprite ($Cu_2O$) are two stable phases in copper oxides at an ambient environment. As *p*-type semiconductors, CuO and $Cu_2O$ separately possess a band gap of 1.9–2.1 and 2.1–2.6 eV [61]. Both binary copper oxides are

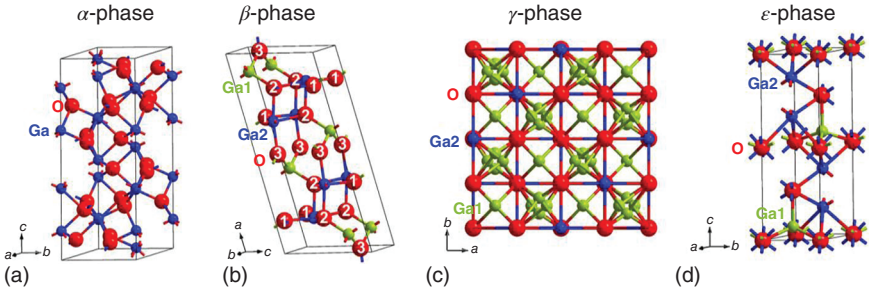


**Figure 1.6** Crystal structure $Ga_2O_3$ polymorphs. (a) Rhombohedral crystal structure of corundum-like $\alpha$-$Ga_2O_3$. (b) Monoclinic $\beta$-$Ga_2O_3$ crystal structure. (c) Cubic defective spinel lattice structure of $\gamma$-phase $Ga_2O_3$. (d) Orthorhombic $\varepsilon$-$Ga_2O_3$ structure. Source: Reproduced from Zhang et al. [53]/with permission of AIP Publishing.

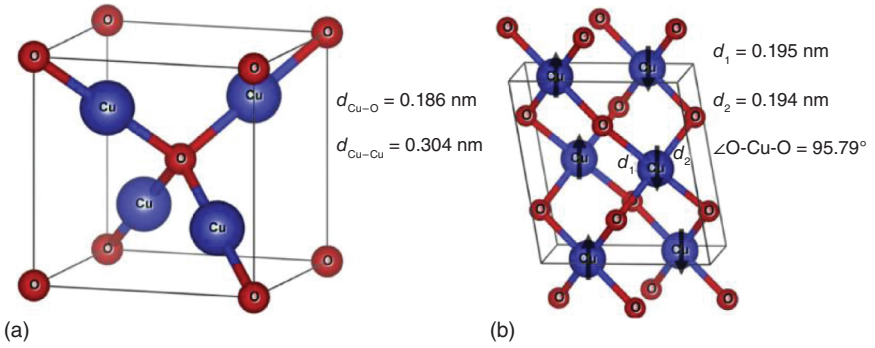


**Figure 1.7** Crystal structure of binary copper oxides. (a) Cubic $Cu_2O$ and (b) Monoclinic CuO. Source: Reproduced from Gupta et al. [61]/with permission of Elsevier.

attractive for versatile applications such as solar cells, TFTs, gas sensors, and photoelectric detectors [62–67]. When annealed at a high temperature, $Cu_2O$ could transform to CuO by the oxidation reaction [63]. In addition to these two stable phases, paramelaconite ($Cu_4O_3$) is another metastable mixed-valence intermediate compound between $Cu_2O$ and CuO and could decompose into $Cu_2O$ and CuO beyond the stability limit under vacuum environment at 670–800 K. Figure 1.7 illustrates these crystal structures of $Cu_2O$ and CuO [61].

### 1.3.2 SnO

Recently, tin monoxide (SnO) has garnered significant attention due to its inherent *p*-type conductivity, structural stability, and electric properties in ambient environment [68]. The bandgap of SnO ranges from 2.2 to 3.0 eV at 300 K [69]. Figure 1.8 illustrates the crystal structure of SnO and the hybridization of valence-band maximum (VBM) [62]. It is worth noting that the energy level of Sn 5*s* is in close proximity to that of O 2*p* near the VBM, as well as Sn 5*p* near the conduction band. This arrangement effectively reduces hole localization and results in high hole

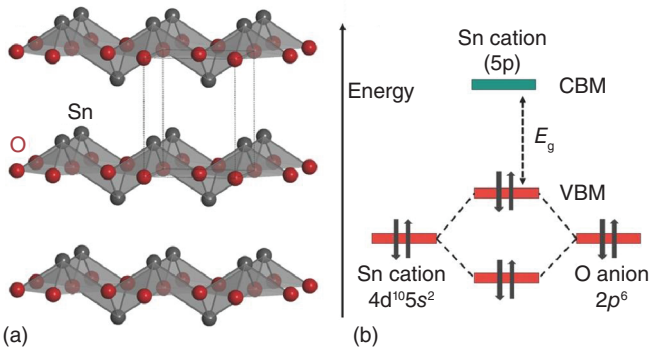


**Figure 1.8** (a) Crystal structure of SnO. (b) Schematic illustration of the valence-band maximum (VBM) hybridization in SnO. Source: Reproduced from Wang et al. [62]/with permission of Elsevier.

mobility. The presence of Sn vacancies and oxygen interstitials contributes to the *p*-type conductivity observed in SnO [70]. The native *p*-type behavior of SnO makes it suitable for various applications in the fields of TFTs [71], gas sensors [72], and optoelectronics [69].

### 1.3.3 $NiO_x$

$NiO_x$ is a widely studied *p*-type semiconductor that exhibits a green color in ambient environments and possesses a wide bandgap ranging from 3.6 to 4.0 eV [73]. Due to its exceptional thermodynamic stability and unique optical/chemical properties [74, 75], $NiO_x$ has attracted significant research interest in various fields, including solar cells [76], supercapacitors [77], catalysis [78], electrodes for lithium-ion batteries [74], and gas sensors [79].

Figure 1.9a illustrates the crystal structure of NiO. Nalage et al. proposed a sol–gel synthesis method for NiO thin films [80]. In this typical procedure, nickel acetate serves as the source of Ni, and the flow diagram for the production of NiO films is depicted in Figure 1.9b. The NiO films prepared through this process and subsequently sintered at 700 °C exhibited an electron carrier concentration and mobility of $3.75 \times 10^{19}$ $cm^{-3}$ and $4.2 \times 10^{-5}$ $cm^2$ $V^{-1}s^{-1}$, respectively, along with a bandgap of 3.47 eV.

In various application scenarios like TFTs, photocatalysts, gas sensors, solar cells, and memristors, the morphological and structural characteristics of metal oxides play a crucial role in determining their performance. Factors such as crystal phases, terminal atom species, crystal size, shape, defects, vacancies, and crystal planes significantly influence the ultimate performance of these materials. Therefore, depending on the desired performance requirements, it is possible to design and improve the synthesis parameters while adhering to a fixed preparation strategy. This approach allows us to obtain the desired metal oxide with specific properties, albeit with some compromises between performance merits such as sensitivity and stability.

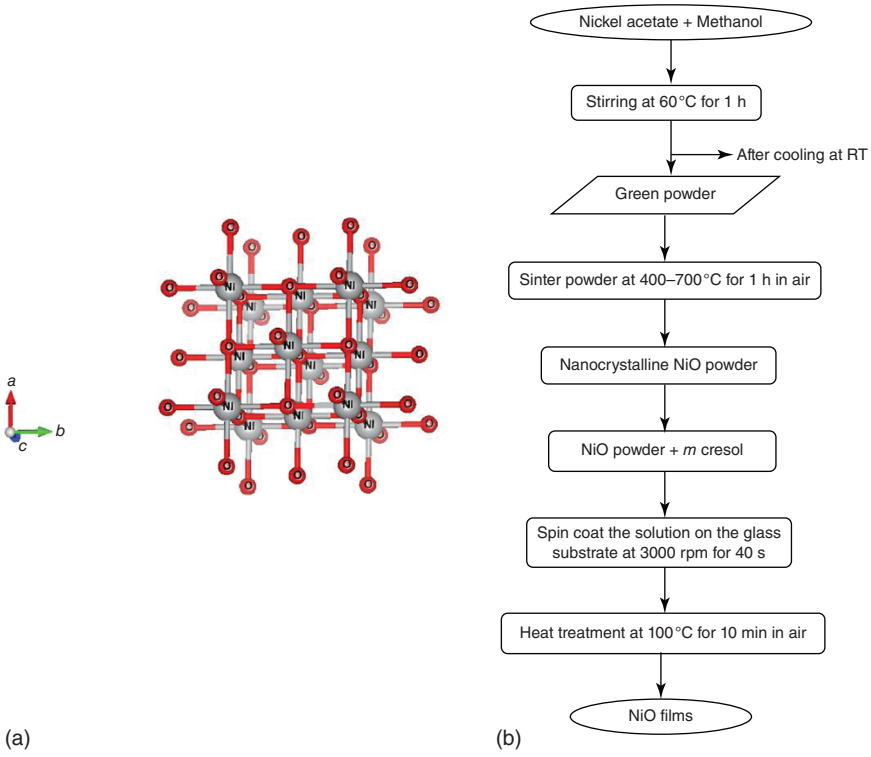


**Figure 1.9** (a) Crystal structure of $NiO_x$. Source: Reproduced from Goel et al. [75]/with permission of Elsevier. Copyright 2020, Elsevier. (b) Flow diagram for NiO films synthesis by sol–gel method. Source: Reproduced from Nalage et al. [80]/with permission of Elsevier.

## References


1 Yu, X., Marks, T., and Facchetti, A. (2016). Metal oxides for optoelectronic applications. *Nat. Mater.* 15 (4): 383–396.

2 Karthikeyan, C., Arunachalam, P., Ramachandran, K. et al. (2020). Recent advances in semiconductor metal oxides with enhanced methods for solar photocatalytic applications. *J. Alloys Compd.* 828: 154281.

3 Valdes, A., Brillet, J., Gratzel, M. et al. (2012). Solar hydrogen production with semiconductor metal oxides: new directions in experiment and theory. *Phys. Chem. Chem. Phys.* 14 (1): 49–70.

4 Khan, M., Adil, S., and Al-Mayouf, A. (2015). Metal oxides as photocatalysts. *J. Saudi Chem. Soc.* 19 (5): 462–464.

5 Jose, R., Thavasi, V., and Ramakrishna, S. (2009). Metal oxides for dye-sensitized solar cells. *J. Am. Ceram. Soc.* 92 (2): 289–301.

6 Park, J., Maeng, W., Kim, H. et al. (2012). Review of recent developments in amorphous oxide semiconductor thin-film transistor devices. *Thin Solid Films* 520 (6): 1679–1693.

7 Mohammad, B., Jaoude, M., Kumar, V. et al. (2016). State of the art of metal oxide memristor devices. *Nanotechnol. Rev.* 5 (3): 311–329.

8 Barsan, N., Koziej, D., and Weimar, U. (2007). Metal oxide-based gas sensor research: how to? *Sens. Actuators, B* 121 (1): 18–35.

9 Ping, Y., Goddard, W., and Galli, G. (2015). Energetics and solvation effects at the photoanode/catalyst interface: ohmic contact versus schottky barrier. *J. Am. Chem. Soc.* 137 (16): 5264–5267.

10 Sun, Y., Yan, X., Zheng, X. et al. (2015). High on–off ratio improvement of ZnO-based forming-free memristor by surface hydrogen annealing. *ACS Appl. Mater. Interfaces* 7 (13): 7382–7388.

11 Afouxenidis, D., Mazzocco, R., Vourlias, G. et al. (2015). ZnO-based thin film transistors employing aluminum titanate gate dielectrics deposited by spray pyrolysis at ambient air. *ACS Appl. Mater. Interfaces* 7 (13): 7334–7341.

12 Wang, M., Han, J., Hu, Y. et al. (2016). Carbon-incorporated NiO/$TiO_2$ mesoporous shells with p-n heterojunctions for efficient visible light photocatalysis. *ACS Appl. Mater. Interfaces* 8 (43): 29511–29521.

13 Cho, I., Sim, Y., Cho, M. et al. (2020). Monolithic micro light-emitting diode/metal oxide nanowire gas sensor with microwatt-level power consumption. *ACS Sens.* 5 (2): 563–570.

14 Kaphle, A., Echeverria, E., McLlroy, D. et al. (2020). Enhancement in the performance of nanostructured CuO-ZnO solar cells by band alignment. *RSC Adv.* 10 (13): 7839–7854.

15 Szczuko, D., Werner, J., Oswald, S. et al. (2001). XPS investigations of surface segregation of doping elements in $SnO_2$. *Appl. Surf. Sci.* 179 (1–4): 301–306.

16 Kılıç, Ç. and Zunger, A. (2002). Origins of coexistence of conductivity and transparency in $SnO_2$. *Phys. Rev. Lett.* 88 (9): 095501.

17 Guo, D., Guo, Q., Chen, Z. et al. (2019). Review of $Ga_2O_3$-based optoelectronic devices. *Mater. Today Phys.* 11: 100157.

18 Hashimoto, K., Irie, H., and Fujishima, A. (2005). $TiO_2$ photocatalysis: a historical overview and future prospects. *Jpn. J. Appl. Phys.* 44 (12R): 8269–8285.

19 Klingshirn, C. (2007). ZnO: material, physics and applications. *ChemPhysChem* 8 (6): 782–803.

20 Wang, H. and Rogach, A. (2014). Hierarchical $SnO_2$ nanostructures: recent advances in design, synthesis, and applications. *Chem. Mater.* 26 (1): 123–133.

21 Lim, S., Hwang, S., Chang, D. et al. (2010). Preparation of mesoporous $In_2O_3$ nanofibers by electrospinning and their application as a CO gas sensor. *Sens. Actuators, B* 149 (1): 28–33.

22 Kastner, M., Birgeneau, R., Shirane, G. et al. (1998). Magnetic, transport, and optical properties of monolayer copper oxides. *Rev. Mod. Phys.* 70 (3): 897–928.

23 Saji, K., Venkata, S.Y., Tian, K. et al. (2016). P-type SnO thin films and SnO/ZnO heterostructures for all-oxide electronic and optoelectronic device applications. *Thin Solid Films* 605: 193–201.

**24** Silva, V., Simões, T., Grilo, J. et al. (2020). Impact of the NiO nanostructure morphology on the oxygen evolution reaction catalysis. *J. Mater. Sci.* 55: 6648–6659.

**25** Huang, F., Lin, Z., Lin, W. et al. (2014). Research progress in ZnO single-crystal: growth, scientific understanding, and device applications. *Chin. Sci. Bull.* 59: 1235–1250.

**26** Wang, Z. (2004). Zinc oxide nanostructures: growth, properties and applications. *J. Phys. Condens. Matter* 16 (25): 829–858.

**27** Janotti, A. and Van de Walle, C. (2009). Fundamentals of zinc oxide as a semiconductor. *Rep. Prog. Phys.* 72 (12): 126501.

**28** Wang, Z. (2007). Novel nanostructures of ZnO for nanoscale photonics, optoelectronics, piezoelectricity, and sensing. *Appl. Phys. A* 88: 7–15.

**29** Harun, K., Hussain, F., Purwanto, A. et al. (2017). Sol–gel synthesized ZnO for optoelectronics applications: a characterization review. *Mater. Res. Express* 4 (12): 122001.

**30** Tian, C., Zhang, Q., Wu, A. et al. (2012). Cost-effective large-scale synthesis of ZnO photocatalyst with excellent performance for dye photodegradation. *Chem. Commun.* 48 (23): 2858–2860.

**31** Hsiao, C., Hu, Y., Chang, R. et al. (2009). Residual stresses and mechanical properties of a ZnO pyroelectric sensor. *Theor. Appl. Fract. Mech.* 52 (1): 1–6.

**32** Dhiman, P., Rana, G., Kumar, A. et al. (2022). ZnO-based heterostructures as photocatalysts for hydrogen generation and depollution: a review. *Environ. Chem. Lett.* 20: 1047–1081.

**33** Yi, G., Wang, C., and Park, W. (2005). ZnO nanorods: synthesis, characterization and applications. *Semicond. Sci. Technol.* 20 (4): 22.

**34** Akgul, F., Gumus, C., Er, A. et al. (2013). Structural and electronic properties of $SnO_2$. *J. Alloys Compd.* 579: 50–56.

**35** Das, S. and Jayaraman, V. (2014). $SnO_2$: a comprehensive review on structures and gas sensors. *Prog. Mater Sci.* 66: 112–255.

**36** El-Etre, A. and Reda, S. (2010). Characterization of nanocrystalline $SnO_2$ thin film fabricated by electrodeposition method for dye-sensitized solar cell application. *Appl. Surf. Sci.* 256 (22): 6601–6606.

**37** Kar, A., Sain, S., Kundu, S. et al. (2015). Influence of size and shape on the photocatalytic properties of $SnO_2$ nanocrystals. *ChemPhysChem* 16 (5): 1017–1025.

**38** Srivastava, A. (2003). Detection of volatile organic compounds (VOCs) using $SnO_2$ gas-sensor array and artificial neural network. *Sens. Actuators, B* 96 (1–2): 24–37.

**39** Yadava, Y., Denicoló, G., Arias, A. et al. (1997). Preparation and characterization of transparent conducting tin oxide thin film electrodes by chemical vapour deposition from reactive thermal evaporation of $SnCl_2$. *Mater. Chem. Phys.* 48 (3): 263–267.

**40** Gracia, L., Beltrán, A., and Andrés, J. (2007). Characterization of the high-pressure structures and phase transformations in $SnO_2$. A density functional theory study. *J. Phys. Chem. B* 111 (23): 6479–6485.

**41** Spencer, J., Mock, A., Jacobs, A. et al. (2022). A review of band structure and material properties of transparent conducting and semiconducting oxides: $Ga_2O_3$, $Al_2O_3$, $In_2O_3$, ZnO, $SnO_2$, CdO, NiO, CuO, and $Sc_2O_3$. *Appl. Phys. Rev.* 9 (1): 011315.

**42** Zhang, K., Lazarov, V., Galindo, P. et al. (2012). Domain matching epitaxial growth of $In_2O_3$ thin films on α-$Al_2O_3$(0001). *Cryst. Growth Des.* 12 (2): 1000–1007.

**43** Roy, P., Berger, S., and Schmuki, P. (2011). $TiO_2$ nanotubes: synthesis and applications. *Angew. Chem. Int. Ed. Engl.* 50 (13): 2904–2939.

**44** Chen, X. and Selloni, A. (2014). Introduction: titanium dioxide ($TiO_2$) nanomaterials. *Chem. Rev.* 114 (19): 9281–9282.

**45** Siegel, R., Ramasamy, S., Hahn, H. et al. (2011). Synthesis, characterization, and properties of nanophase $TiO_2$. *J. Mater. Res.* 3 (6): 1367–1372.

**46** Kusior, A., Banas, J., Trenczek-Zajac, A. et al. (2018). Structural properties of $TiO_2$ nanomaterials. *J. Mol. Struct.* 1157: 327–336.

**47** Garzella, C., Comini, E., Tempesti, E. et al. (2000). $TiO_2$ thin films by a novel sol–gel processing for gas sensor applications. *Sens. Actuators, B* 68 (1–3): 189–196.

**48** Wang, Z., Yamaguchi, T., Sugihara, H. et al. (2005). Significant efficiency improvement of the black dye-sensitized solar cell through protonation of $TiO_2$ films. *Langmuir* 21 (10): 4272–4276.

**49** Nakata, K. and Fujishima, A. (2012). $TiO_2$ photocatalysis: design and applications. *J. Photochem. Photobiol. C* 13 (3): 169–189.

**50** Bai, J. and Zhou, B. (2014). Titanium dioxide nanomaterials for sensor applications. *Chem. Rev.* 114 (19): 10131–10176.

**51** Macwan, D., Dave, P., and Chaturvedi, S. (2011). A review on nano-$TiO_2$ sol–gel type syntheses and its applications. *J. Mater. Sci.* 46: 3669–3686.

**52** Linsebigler, A., Lu, G., and Yates, J. (1995). Photocatalysis on $TiO_2$ surfaces: principles, mechanisms, and selected results. *Chem. Rev.* 95 (3): 735–758.

**53** Zhang, J., Shi, J., Qi, D. et al. (2020). Recent progress on the electronic structure, defect, and doping properties of $Ga_2O_3$. *APL Mater.* 8 (2): 020906.

**54** Pearton, S., Yang, J., Cary, P. et al. (2018). A review of $Ga_2O_3$ materials, processing, and devices. *Appl. Phys. Rev.* 5 (1): 011301.

**55** Higashiwaki, M., Sasaki, K., Murakami, H. et al. (2016). Recent progress in $Ga_2O_3$ power devices. *Semicond. Sci. Technol.* 31 (3): 034001.

**56** Zhang, M., Kang, S., Wang, L. et al. (2021). Facile synthesis of β–$Ga_2O_3$ nanowires network for solar-blind ultraviolet photodetector. *J. Phys. D: Appl. Phys.* 54 (17): 175106.

**57** Ping, L., Berhanuddin, D., Mondal, A. et al. (2021). Properties and perspectives of ultrawide bandgap $Ga_2O_3$ in optoelectronic applications. *Chin. J. Phys.* 73: 195–212.

**58** Galazka, Z. (2018). β-$Ga_2O_3$ for wide-bandgap electronics and optoelectronics. *Semicond. Sci. Technol.* 33 (11): 113001.

**59** Liang, H., Cui, S., Su, R. et al. (2018). Flexible X-ray detectors based on amorphous $Ga_2O_3$ thin films. *ACS Photonics* 6 (2): 351–359.

**60** Wang, C., Zhang, J., Xu, S. et al. (2021). Progress in state-of-the-art technologies of $Ga_2O_3$ devices. *J. Phys. D: Appl. Phys.* 54 (24): 243001.

**61** Gupta, D., Meher, S., Illyaskutty, N. et al. (2018). Facile synthesis of $Cu_2O$ and CuO nanoparticles and study of their structural, optical and electronic properties. *J. Alloys Compd.* 743: 737–745.

**62** Wang, Z., Nayak, P., Caraveo-Frescas, J. et al. (2016). Recent developments in p-type oxide semiconductor materials and devices. *Adv. Mater.* 28 (20): 3831–3892.

**63** Al-Jawhari, H. (2015). A review of recent advances in transparent p-type $Cu_2O$-based thin film transistors. *Mater. Sci. Semicond. Process.* 40: 241–252.

**64** Teng, F., Hu, K., Ouyang, W. et al. (2018). Photoelectric detectors based on inorganic p-type semiconductor materials. *Adv. Mater.* 30 (35): 1706262.

**65** Kim, H. and Lee, J. (2014). Highly sensitive and selective gas sensors using p-type oxide semiconductors: overview. *Sens. Actuators, B* 192: 607–627.

**66** Zhang, Q., Zhang, K., Xu, D. et al. (2014). CuO nanostructures: synthesis, characterization, growth mechanisms, fundamental properties, and applications. *Prog. Mater Sci.* 60: 208–337.

**67** Grigore, M., Biscu, E., Holban, A. et al. (2016). Methods of synthesis, properties and biomedical applications of CuO nanoparticles. *Pharmaceuticals* 9 (4): 75.

**68** Allen, J., Scanlon, D., Piper, L. et al. (2013). Understanding the defect chemistry of tin monoxide. *J. Mater. Chem. C.* 1 (48): 8194–8208.

**69** Singh, M., Gaspera, E., Ahmed, T. et al. (2017). Soft exfoliation of 2D SnO with size-dependent optical properties. *2D Mater.* 4 (2): 025110.

**70** Eqbal, E. and Anila, E. (2018). Properties of transparent conducting tin monoxide(SnO) thin films prepared by chemical spray pyrolysis method. *Physica B* 528: 60–65.

**71** Yabuta, H., Kaji, N., Hayashi, R. et al. (2010). Sputtering formation of p-type SnO thin-film transistors on glass toward oxide complimentary circuits. *Appl. Phys. Lett.* 97 (7): 072111.

**72** Suman, P., Felix, A., Tuller, H. et al. (2015). Comparative gas sensor response of $SnO_2$, SnO and $Sn_3O_4$ nanobelts to $NO_2$ and potential interferents. *Sens. Actuators, B* 208: 122–127.

**73** Mokoena, T., Swart, H., and Motaung, D. (2019). A review on recent progress of p-type nickel oxide based gas sensors: future perspectives. *J. Alloys Compd.* 805: 267–294.

**74** Varghese, B., Reddy, M., Yanwu, Z. et al. (2008). Fabrication of NiO nanowall electrodes for high performance lithium ion battery. *Chem. Mater.* 20 (10): 3360–3367.

**75** Goel, R., Jha, R., and Ravikant, C. (2020). Investigating the structural, electrochemical, and optical properties of p-type spherical nickel oxide (NiO) nanoparticles. *J. Phys. Chem. Solids* 144: 109488.

**76** Kaviyarasu, K., Manikandan, E., Kennedy, J. et al. (2016). Synthesis and characterization studies of NiO nanorods for enhancing solar cell efficiency using photon upconversion materials. *Ceram. Int.* 42 (7): 8385–8394.

**77** Kate, R., Khalate, S., and Deokate, R. (2018). Overview of nanostructured metal oxides and pure nickel oxide (NiO) electrodes for supercapacitors: a review. *J. Alloys Compd.* 734: 89–111.

**78** Wu, J., Huang, Y., Xia, Q. et al. (2013). Decomposition of toluene in a plasma catalysis system with NiO, $MnO_2$, $CeO_2$, $Fe_2O_3$, and CuO catalysts. *Plasma Chem. Plasma Process.* 33: 1073–1082.

**79** Zhou, Q., Lu, Z., Wei, Z. et al. (2018). Hydrothermal synthesis of hierarchical ultrathin NiO nanoflakes for high-performance $CH_4$ sensing. *Front. Chem.* 6: 194.

**80** Nalage, S., Chougule, M., Sen, S. et al. (2012). Sol–gel synthesis of nickel oxide thin films and their characterization. *Thin Solid Films* 520 (15): 4835–4840.